INDERSCIENCE PUBLISHERS
Linking academia, business and industry through research

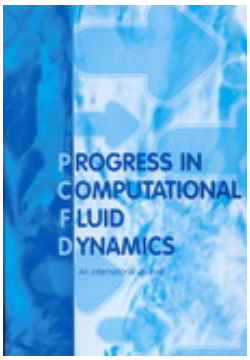

Progress in Computational Fluid Dynamics, An International Journal

ISSN online: 1741-5233 - ISSN print: 1468-4349
https://www.inderscience.com/pcfd

Investigation of the flow topology evolution between two tandem cylinders using a discontinuous Galerkin method

Xiangjun Shan, Fangjin Sun

DOI: 10.1504/PCFD.2024.10060947

Article History:

Received:	25 June 2021
Last revised:	26 July 2022
Accepted:	24 October 2022
Published online:	20 December 2023

Investigation of the flow topology evolution between two tandem cylinders using a discontinuous Galerkin method

Xiangjun Shan* and Fangjin Sun

School of Mechanics and Engineering,
Liaoning Technical University,
Fuxin, 123000, China
Email: x_j_shan@outlook.com
Email: e_dm@163.com
*Corresponding author

Abstract: A high-order discontinuous Galerkin method is used to study the transient behaviour of the flow between two cylinders in a tandem arrangement. A low Reynolds number of 200 and a pitch ratio of 3.7 are particularly employed, where a gradual transition process of the flow from reattachment flow to co-shedding flow is observed. The evolution of the flow topology in the gap between two cylinders, the transient surface pressure and the phase lag of the lift signal from reattachment flow to co-shedding flow are investigated, and the physical mechanism responsible for the flow transition is also discussed. The results show that the rolling up of the separated shear layer between two cylinders is closely related to the development of the gap flow. The gap flow is a unidirectional flow in the reattachment regime and gradually develops into a 'horseshoe-shaped' bidirectional flow when the flow transitions to the co-shedding regime.

Keywords: discontinuous Galerkin method; higher-order accuracy; tandem cylinders; low Reynolds number; transient characteristics; incompressible flow.

Reference to this paper should be made as follows: Shan, X. and Sun, F. (2024) 'Investigation of the flow topology evolution between two tandem cylinders using a discontinuous Galerkin method', *Progress in Computational Fluid Dynamics*, Vol. 24, No. 1, pp.29–41.

Biographical notes: Xiangjun Shan is currently a PhD candidate in the Department of Mechanics and Engineering at Liaoning Technical University. His research interests are the problems of fluid-solid interaction and the application of discontinuous Galerkin methods for fluid dynamics.

Fangjin Sun is currently a Professor in the Department of Civil and Architectural Engineering of Guilin University of Technology. She received her PhD in Mechanics and Engineering from the Liaoning Technical University. Her research fields are numerical methods and multiphase flow simulation for fluid structure interaction problems.

1 Introduction

In many engineering applications, such as high-rise buildings or skyscrapers, chemical-reaction towers, chimney stacks, submarine communication systems, electronic components on boards, overhead power-line bundles, undersea piggyback pipelines, drilling risers, tube bundles in heat exchangers, bridge piers, stays and masts, are directly related to unsteady flow past multiple slender structures. As the basis of understanding the flow around multiple cylinders with complex arrangements, the flow around two tandem cylinders involves the most generic flow characteristics, including flow separation, shear-layer development, quasiperiodic vortices, gap flow switching, separation bubbles, mutual interactions, vortex impingement, etc. Therefore, as an excellent model for gaining insight into the flow physics of multiple cylindrical structures, the flow around and forces on two tandem cylinders have been widely studied (Grioni et al., 2020; Yang and Stremler, 2019; Zhou et al., 2019; Zhou and Alam, 2016).

The flow around two tandem cylinders is highly dependent on the separation $l^* = L/D$ (i.e., the ratio of the centre-to-centre distance between the cylinders to the diameter of the two cylinders). It is well known that this flow can be classified into a reattachment regime and co-shedding regime according to whether the shear layer separated from the upstream cylinder is reattached to the downstream cylinder or rolled up in the gap between the two cylinders (Igarashi and Suzuki, 1984; Zdravkovich, 1987; Zdravkovich and Pridden, 1977). In the reattachment regime ($1.2\sim1.8 < l^* < 3.4\sim3.8$), although no vortices shed off from the upstream cylinder, the flow between the two cylinders was non-uniform. The shear layer separated from the upstream cylinder is divided when reattached to the surface of the downstream cylinder, and part of the shear

layer turns toward the upstream cylinder and forms a region of circumfluence in the gap, while the other part continues downstream and shed off behind the downstream cylinder. In the co-shedding regime ($l^* > 3.4$~3.8), vortex shedding occurs from both cylinders. The separated shear layers are alternately rolled up to form vortices between the cylinders and interact strongly with the vortex shedding of the downstream cylinder. There is a bistable flow between the reattachment and co-shedding regimes, where both reattachment and co-shedding flows switch intermittently from one to the other. The corresponding l^* is often referred to as the critical spacing l_c^* (Igarashi and Suzuki, 1984; Xu and Zhou, 2004; Zdravkovich, 1985). When the flow changes from the reattachment to the co-shedding regimes ($l^* > l_c^*$), the fluid dynamics around the two tandem cylinders will be changed. For example, the length of the recirculation bubble behind the downstream cylinder decreases (Lin et al., 2002; Zhou et al., 2019), the time-averaged drag of the downstream cylinder changes from a negative value to a positive value (Meneghini et al., 2001; Singha and Sinhamahapatra, 2010), and the Strouhal number *St*, fluctuating drag and fluctuating lift of the two cylinders increase (Grioni et al., 2020; Zhou et al., 2019).

Previous studies on the flow around two tandem cylinders usually considered the reattachment and co-shedding regimes as two independent cases and studied the fluid forces and flow structure in a statistical sense. However, there are few reports on the evolution of the flow structure and the corresponding instantaneous characteristics during the transition from reattachment flow to co-shedding flow, although it is of great significance for further understanding the bistable flow and the flow physics around tandem cylinders. The study of this instantaneous characteristic requires high sensitivity for the experimental device and high accuracy for the numerical method.

With the rapid development of computing power, many numerical methods have been used to study the flow around two tandem cylinders (Carmo et al., 2010a, 2010b; Grioni et al., 2020; Zhang et al., 2018; Zhou et al., 2019). In the last few years, the discontinuous Galerkin (DG) method has become an increasingly important and efficient high-order method, especially in the field of hydrodynamics. This method combines two key ideas of both the finite volume method and finite element method to solve the Riemann problem at the interface and uses the high-order polynomial approximation solution to obtain the precision in the element. DG allows local refinement by variable polynomial order and element size, so it can deal with complex geometry. Using the DG method, Niroobakhsh et al. (2017) investigated vortex shedding in the wakes of a circular cylinder and a NACA 0012 airfoil. Chen et al. (2020) investigated a flow around a cylinder that lies inside a channel. Similar studies also include Zhang et al. (2021), Fu and Wang (2020), Zhang et al. (2020) and Ferrero and Larocca (2016). We have successfully analysed the flow topology of two tandem cylinders using the DG method, but only the reattachment regime was considered (Shan and Sun, 2021). To the best of the author's knowledge, there are few references to the application of DG to the flow around two tandem cylinders.

The purpose of this work is to simulate the transition from reattachment to co-shedding flow of tandem cylinders by using the high-order DG method to capture the high-resolution instantaneous flow structure and analyse the evolution of the flow topology. To obtain a clear topological image and facilitate comparison with published results, Re = 200 was used. In addition, by observing the time history of the lift coefficient at different l^*, we observed a gradual transition from reattachment flow to co-shedding flow at $l^* = 3.7$. Therefore, we study the transient flow at this spacing. The remainder of this paper is arranged as follows: Section 2 introduces the numerical method, which is verified in Section 3. Descriptions of the reattachment and co-shedding flow, the evolution of the flow topology and the transient dynamic properties are presented in Subsections 4.1, 4.2, and 4.3, respectively. Subsection 4.4 explores the mechanism responsible for the flow transition, and the results are concluded in Section 5.

2 Numerical method

The non-dimensional incompressible Navier-Stokes equations can be expressed mathematically as:

$$\nabla \cdot \mathbf{u} = 0, \tag{1}$$

$$\frac{\partial \mathbf{u}}{\partial t} + (\mathbf{u} \cdot \nabla)\mathbf{u} = -\nabla p + \frac{1}{\mathrm{Re}}\nabla^2 \mathbf{u}. \tag{2}$$

where $\mathbf{u} = (u, v)^T$ is the velocity vector, t is the time, p is the pressure, and Re is the Reynolds number (i.e., $\mathrm{Re} = UL/\nu$, where ν is the kinematic viscosity and U and L represent the characteristic velocity and length, respectively).

2.1 Temporal discretisation

The time discretisation of the governing equations adopts a second-order dual stiffly stable method (Karniadakis et al., 1991), and the momentum equation is given by the following formula:

$$\begin{aligned} &\frac{\gamma_0 \mathbf{u}^{n+1} - \alpha_0 \mathbf{u}^n - \alpha_1 \mathbf{u}^{n-1}}{\Delta t} \\ &= -\nabla p^{n+1} - \beta_0 \left[(\mathbf{u}^n \cdot \nabla)\mathbf{u}^n\right] \\ &-\beta_1 \left[(\mathbf{u}^{n-1} \cdot \nabla)\mathbf{u}^{n-1}\right] + \frac{1}{\mathrm{Re}}\nabla^2 \mathbf{u}^{n+1}, \end{aligned} \tag{3}$$

where the indices $n-1$, n and $n+1$ are the consecutive time steps separated by an increment Δt in time, and γ_0, α_0, α_1, β_0 and β_1 are constants chosen to achieve the desired level of temporal accuracy. By introducing intermediate variables in the present scheme, the incompressible Navier-Stokes equations can be split into three distinct equations, i.e., an explicit nonlinear convection equation, a Poisson equation for pressure and a Helmholtz equation for viscous diffusion. These equations can be solved successively at each time step.

First, by introducing an intermediate velocity $\tilde{\mathbf{u}}$ and using the Adams-Bashforth second-order scheme, the nonlinear convection term can be written as:

$$\begin{aligned}&\frac{\gamma_0\tilde{\mathbf{u}}-\alpha_0\mathbf{u}^n-\alpha_1\mathbf{u}^{n-1}}{\Delta t}\\&=-\beta_0\left[(\mathbf{u}^n\cdot\nabla)\mathbf{u}^n\right]-\beta_1\left[(\mathbf{u}^{n-1}\cdot\nabla)\mathbf{u}^{n-1}\right],\end{aligned}\tag{4}$$

where $\gamma_0 = 3/2$, $\alpha_0 = 2$, $\alpha_1 = -1/2$, $\beta_0 = 2$ and $\beta_1 = -1$. Since this second-order scheme is not self-starting, $\gamma_0 = \alpha_0 = \beta_0 = 1$ and $\alpha_1 = \beta_1 = 0$ are initially required, which reduces the scheme to the first-order explicit forward Euler method.

Second, the pressure term is treated implicitly, and the non-divergence constraint is imposed on the intermediate velocity to obtain the Poisson equation of pressure. We introduce a second divergence-free intermediate velocity $\tilde{\tilde{\mathbf{u}}}$ and write:

$$\gamma_0\frac{\tilde{\tilde{\mathbf{u}}}-\tilde{\mathbf{u}}}{\Delta t}=-\nabla p^{n+1}.\tag{5}$$

We take the divergence of equation (5) and apply $\nabla\cdot\tilde{\tilde{\mathbf{u}}}=0$ to obtain:

$$-\gamma_0\frac{1}{\Delta t}\nabla\cdot\tilde{\mathbf{u}}=-\nabla^2 p^{n+1}.\tag{6}$$

This Poisson problem can be closed by a Neumann boundary condition at inflow and wall boundaries which can be obtained by taking the dot product of the momentum equation with the outward normal vector n at the boundaries:

$$\begin{aligned}\frac{\partial p^{n+1}}{\partial n}=&-\beta_0\mathbf{n}\cdot\left(\frac{\partial\mathbf{u}^n}{\partial t}+(\mathbf{u}^n\cdot\nabla)\mathbf{u}^n+\frac{1}{\mathrm{Re}}\nabla\times\omega^n\right)\\&-\beta_1\mathbf{n}\cdot\left(\frac{\partial\mathbf{u}^{n-1}}{\partial t}+(\mathbf{u}^{n-1}\cdot\nabla)\mathbf{u}^{n-1}+\frac{1}{\mathrm{Re}}\nabla\times\omega^{n-1}\right),\end{aligned}\tag{7}$$

where $\omega = \nabla\times\mathbf{u}$ represents the vorticity and the identity ($\nabla^2\mathbf{u} = -\nabla\times\nabla\times\mathbf{u} = -\nabla\times\omega$) for incompressible flow is used. The intermediate velocity $\tilde{\tilde{\mathbf{u}}}$ in equation (5) is updated by the solution p^{n+1} of the Poisson equation [equation (6)].

Finally, the viscous term is treated implicitly:

$$\gamma_0\left(\frac{\mathbf{u}^{n+1}-\tilde{\tilde{\mathbf{u}}}}{\Delta t}\right)=\frac{1}{\mathrm{Re}}\nabla^2\mathbf{u}^{n+1},\tag{8}$$

which can be written as a Helmholtz equation:

$$-\nabla^2\mathbf{u}^{n+1}+\frac{\mathrm{Re}\,\gamma_0}{\Delta t}\mathbf{u}^{n+1}=\frac{\mathrm{Re}\,\gamma_0}{\Delta t}\tilde{\tilde{\mathbf{u}}}.\tag{9}$$

Equation (9) is solved subject to the no-slip condition at the wall boundaries, and the velocity field is developed at the end of the time step $\mathbf{u}^{n+1}$. It is easy to determine that the sum of equations (4), (5) and (8) recovers the equation (3).

2.2 Spatial discretisation

For the convenience of discussion, we first introduce some notation. Let Ω be a polygonal domain in $\mathbb{R}^2$, where the boundary is denoted as $\partial\Omega$, which can be of Dirichlet type ($\partial\Omega_D$) or Neumann type ($\partial\Omega_N$). Defining $\Omega_h = \{tr\}$ as a triangular tessellation of Ω [as shown in Figure 1(a)], the interior and external boundaries are indicated as $\partial\Omega_h^-$ and $\partial\Omega_h^+$, respectively. Within each element *tr*, the approximate solution u_h is expressed as the modal expansion of the basis function $\phi_i(x, y)$:

$$u_h(x,y)=\sum_{i=1}^{N}u_i\phi(x,y),\tag{10}$$

where $x, y \in tr$ and N is the number of modes (degrees of freedom) in each element. The number of modes required to fully define the expansion on triangular elements is $N = (k + 1)(k + 2)/2$, where k is the polynomial order. The interpolated nodes distribution of the element when $k = 6$ is shown in Figure 1(b). The boundary of each $tr \in \Omega_h$ is further defined as ∂tr, and its unit outward normal vector is $\hat{\mathbf{n}}$. The discontinuous approximation space $V_k(\Omega_h)$ is defined as:

$$V_k(\Omega_h)=\left\{\varphi_h\in L^2(\Omega):\forall tr\in\Omega_h,\,\varphi_h\big|_{tr}\in P_k(tr)\right\},\tag{11}$$

where $P_k(tr)$ represents a polynomial space of order less than or equal to k. The vector version of the space is denoted as $V_k^2(\Omega_h)$. We define the jump $[[\cdot]]$ and the average $\{\{\cdot\}\}$ cross the interface between two adjacent elements tr_1 and tr_2 as:

$$[\![\cdot]\!]=(\cdot|_{tr1}-\cdot|_{tr2}),\ \{\{\cdot\}\}=\frac{1}{2}(\cdot|_{tr1}+\cdot|_{tr2}),\tag{12}$$

and at boundary edges it is expressed as:

$$[\![\cdot]\!]=\{\{\cdot\}\}=(\cdot|_{tr1}).\tag{13}$$

The nonlinear terms in the Navier-Stokes equations are approximated by the DG scheme based on the modified Lesaint-Raviart flux (Ferrer and Willden, 2011), where upwinding is performed for the convection dominated flows. Considering the discretised version of the nonlinear term integrated over Ω_h, we find $\mathbf{u}_h \in V_k^2(\Omega_h)$ to satisfy the following equation:

$$\begin{aligned}&\int_{\Omega_h}(\mathbf{u}_h\cdot\nabla\mathbf{u}_h)\cdot\boldsymbol{\varphi}_h dx=\sum_{tr\in\Omega_h}\int_{tr}(\mathbf{u}_h\cdot\nabla\mathbf{u}_h)\cdot\boldsymbol{\varphi}_h dx\\&+\frac{1}{2}\sum_{tr\in\Omega_h}\int_{tr}(\nabla\cdot\mathbf{u}_h)\mathbf{u}_h\cdot\boldsymbol{\varphi}_h dx\\&+\sum_{tr\in\Omega_h}\int_{\partial tr^-}\left|\{\{\mathbf{u}_h\}\}\cdot\hat{\mathbf{n}}\right|\left(\mathbf{u}_h^--\mathbf{u}_h^+\right)\cdot\boldsymbol{\varphi}_h^- ds\\&-\frac{1}{2}\sum_{\Gamma\in\partial\Omega_h^-\cup\partial\Omega_D}\int_{\Gamma}[\![\mathbf{u}_h]\!]\cdot\hat{\mathbf{n}}\{\{\mathbf{u}_h\cdot\boldsymbol{\varphi}_h\}\}ds,\ \forall\varphi_h\in V_k^2(\Omega_h),\end{aligned}\tag{14}$$

where $\mathbf{u}_h^- - \mathbf{u}_h^+$ represents the jump in the direction of the flow, $\boldsymbol{\varphi}_h^-$ is the test function on the side of *tr* coming from the interior and tr^- represents the portion of the boundary where the flow enters the element (i.e., $\{\{\mathbf{u}_h\}\}\cdot\hat{\mathbf{n}} < 0$). The third term on the right hand side is the upwinding term. Explicit treatment of nonlinear terms introduces a Courant-Friedrichs-Lewy (CFL) type restriction on the time step. The CFL estimate for high-order spatial methods leads to $\Delta t < \Delta t_{CFL} = h/Uk^2$ (Ferrer and Willden, 2011), where U is the characteristic velocity, h is the size of the mesh element, and k represents the polynomial order.

Figure 1 Sketch of, (a) typical elements (b) element nodes (k = 6)

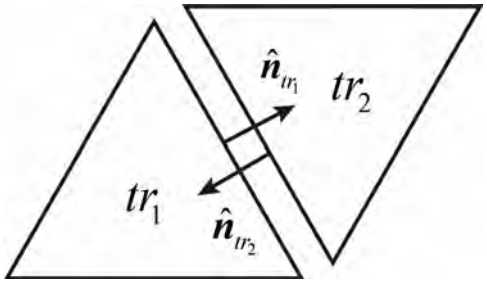

(a)

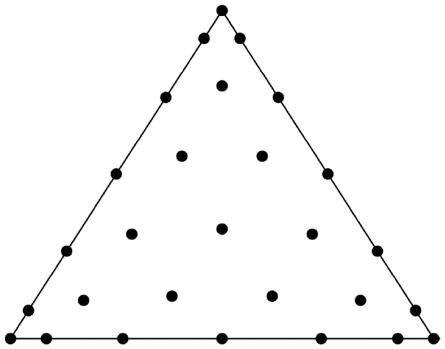

(b)

The time-splitting method described in Subsection 2.1 requires the solution of purely elliptic equations (Poisson and Helmholtz equations) and the symmetric interior penalty Galerkin (SIPG) method is selected to discretise these equations spatially. We present here the general formulation for the continuous elliptic problem:

$$\begin{aligned} &-\Delta u + \alpha u = g \text{ in } \Omega \\ &u = L_D \text{ on } \partial\Omega_D, \\ &\nabla u \cdot \mathbf{n} = L_N \text{ on } \partial\Omega_N, \end{aligned} \tag{15}$$

where $g \in L^2(\Omega)$ is the forcing term, α represents the wave number for the Helmholtz equations, $u \in H^1(\Omega)$ is a scalar (but extension to the vector formulation is direct), n is the outward pointing unit normal vector on $\partial\Omega$, and $L_D \in H^{1/2}(\partial\Omega_h)$ and $L_N \in L^2(\partial\Omega_N)$ indicate the boundary conditions. This form defines the Poisson equation when $g \neq 0$ and $\alpha = 0$, and the Helmholtz equation when $g \neq 0$ and $\alpha \neq 0$.

To find the weak solution of equation (15) using the DG-SIPG method, we introduce the bilinear $a(,)$ and linear $l(\cdot)$ forms, which are associated with the discrete variational formulation resulting from the weak form of the continuous problem (Ferrer and Willden, 2011; Girault and Wheeler, 2008). The bilinear form is defined as:

$$\begin{aligned} a(u_h, \varphi_h) = &\sum_{tr\in\Omega_h}\int_{tr}(\nabla u_h\cdot\nabla\varphi_h)\,dx + \sum_{tr\in\Omega_h}\int_{tr}(\alpha u_h\varphi_h)\,dx \\ &- \sum_{\Gamma\in\partial\Omega_h^+\cup\partial\Omega_D}\int_\Gamma \{\{\nabla u_h\}\}\cdot\hat{\mathbf{n}}[\![\varphi_h]\!]\,ds \\ &- \sum_{\Gamma\in\partial\Omega_h^+\cup\partial\Omega_D}\int_\Gamma \{\{\nabla \varphi_h\}\}\cdot\hat{\mathbf{n}}[\![u_h]\!]\,ds \\ &+ \sum_{\Gamma\in\partial\Omega_h^+\cup\partial\Omega_D}\frac{\sigma}{|trace|^\beta}\int_\Gamma [\![u_h]\!][\![\varphi_h]\!]\,ds, \end{aligned} \tag{16}$$

and the linear form:

$$\begin{aligned} l(\varphi_h) = &\sum_{tr\in\Omega_h}\int_{tr}(g\varphi_h)\,dx \\ &+ \sum_{\Gamma\in\Omega_D}\int_\Gamma\left(-\nabla\varphi_h\cdot\hat{\mathbf{n}} + \frac{\sigma}{|trace|^\beta}\varphi_h\right)L_D\,ds \\ &+ \sum_{\Gamma\in\partial\Omega_N}\int_\Gamma \varphi_h L_N\,ds, \end{aligned} \tag{17}$$

where σ and β are positive real parameters, $\varphi_h \in V_k(\Omega_h)$ and $|trace|$ represents the length of the element edge. Then, the DG-SIPG approximate solution reduces to finding $u_h \in V_k(\Omega_h)$ provided by $a(u_h, \varphi_h) = l(\varphi_h)$, $\forall\varphi_h \in V_k(\Omega_h)$. The combination of σ and β in equations (16) and (17), which define the penalty parameter, must be chosen large enough to enforce the bilinear form (Riviere, 2008).

2.3 Definitions of characteristic quantities

The Reynolds number and Strouhal number are defined as:

$$\mathrm{Re} = \frac{u_\infty D}{\nu},\ St = \frac{f u_\infty}{D}, \tag{18}$$

where f represents the frequency of the fluctuation lift and u_∞ is the velocity of the free stream. The mechanical parameters, including the drag coefficient, lift coefficient and pressure coefficient, are defined as follows:

$$C_D(t) = \frac{F_x(t)}{\frac{1}{2}\rho u_\infty^2 D},\ C_L(t) = \frac{F_y(t)}{\frac{1}{2}\rho u_\infty^2 D},\ C_p(t) = \frac{p(t)-p_\infty}{\frac{1}{2}\rho u_\infty^2}. \tag{19}$$

The time-averaged drag coefficient and root-mean-square lift coefficient can be calculated as:

$$\bar{C}_D = \frac{1}{T}\int_0^T C_D(t)dt,\ C'_{L,rms} = \sqrt{\frac{\int_0^T C_L(t)^2\,dt}{T}}. \tag{20}$$

In the above equations, F_x and F_y are the horizontal and vertical components, respectively, of the resultant force on the cylinder, p_∞ is the freestream pressure, and T is the

fluctuation period. In addition, the time-averaged and root-mean-square force coefficients are calculated in a statistically stable time interval. Finally, the dimensionless time, velocity and distance are defined as:

$$t^* = \frac{tu_\infty}{D}, u^* = \frac{u}{u_\infty}, x^* = \frac{x}{D}, y^* = \frac{y}{D}. \quad (21)$$

2.4 Physical model and boundary conditions

Figure 2 provides a schematic of the physical model studied in this paper. The assumed infinitely extended flow field is approximately a rectangular domain. The uniform free stream passes through two equal-diameter cylinders arranged in tandem with a diameter of D at a speed u_∞, and the distance between the two cylinders is $l^* = 3.7$. The distance from the inlet to the centre of the upstream cylinder and from the boundary on both sides to the centreline of the two cylinders is 20D, and the distance from the outlet to the centre of the downstream cylinder is 30D. The size of the computational domain is configured according to the size independence studies of a single cylinder and tandem cylinders by Jiang et al. (2016) and Mizushima and Suehiro (2005), respectively, so the influence of the far-field effect and blockage ratio can be ignored in these dimensions. The boundary conditions are depicted in Figure 2, in which the non-slip boundary is applied to the surfaces of two cylinders. The pressure at the outlet boundary is set to zero, and the remaining boundaries are subject to Neumann-type conditions (Wang et al., 2019). The initial conditions (at $t^* = 0$) are $u/u_\infty = 1$, $v/u_\infty = 0$, and $p/\rho u_\infty^2 = 0$, where u and v are the velocity components in the x and y directions, respectively, in the Cartesian coordinate system.

Figure 2 Schematic of the physical model with boundary conditions

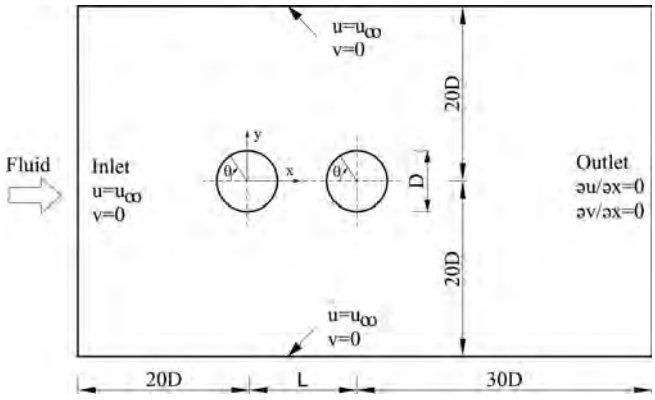

2.5 Grid system

The meshing of the computational domain is illustrated in Figure 3. To better capture the boundary layer and wake structure, the grid is refined along the radial direction and wake direction of the cylinders, as shown in Figure 3(b). The curvilinear boundaries around the cylinder are approximated by deforming the straight-sided faces of the element. Details on the forming of the curvilinear element can be found in the work of Hesthaven and Warburton (2008). The total number of elements is 2,232, and 22 nodes are arranged along the circumference of each cylinder.

Figure 3 Multi-block unstructured grid at $l^* = 3.7$, (a) Meshing of the entire computational domain (b) details near the walls of two cylinders

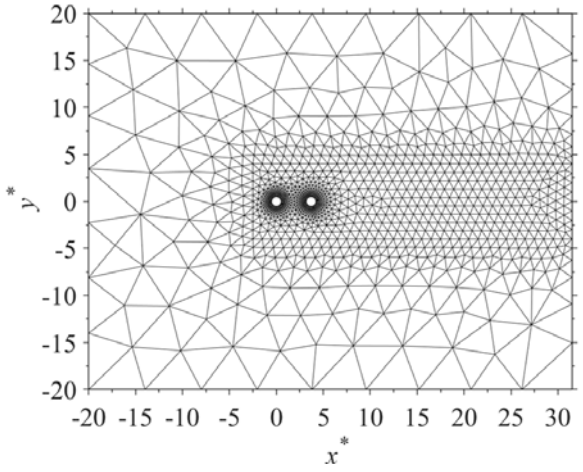

(a)

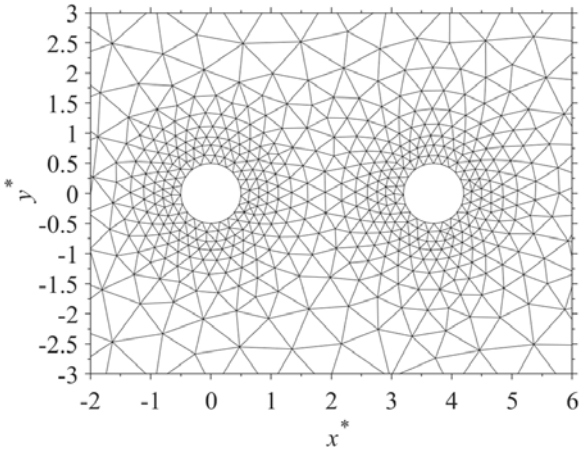

(b)

To ensure the grid independence of the calculation results, the grid resolution is investigated by changing the order of the interpolation polynomial. The physical quantities tested are the time-averaged drag coefficient $\overline{C}_D$, fluctuating (root-mean-square, *rms*) lift coefficient $C'_{L,rms}$, and Strouhal number *St*. The results are shown in Table 1. The subscripts '1' and '2' indicate the upstream and downstream cylinders, respectively. Observations reveal that due to the high accuracy of the numerical method and the reasonable distribution of the mesh, the results change little with increasing polynomial order. Therefore, considering the computing power and numerical accuracy, $N_p = 6$ is used hereafter, which can solve this problem correctly.

Table 1 Grid resolution test results at Re = 200

N_p	$\bar{C}_{D1}$	$\bar{C}_{D2}$	$C'_{L1,rms}$	$C'_{L2,rms}$	St
5	1.22977638	0.35650797	0.56167755	1.17546364	0.17500074
6	1.23741793	0.36132129	0.56087572	1.18837950	0.17500054
7	1.23328905	0.36428096	0.56281038	1.18587283	0.17500030
8	1.23367691	0.36502730	0.56290528	1.18669793	0.17500024

Figure 4 Dependence of the time-averaged drag $\bar{C}_D$ and Strouhal number St of the two cylinders on the pitch ratio l^*, (a) time-averaged drag (b) Strouhal number (see online version for colours)

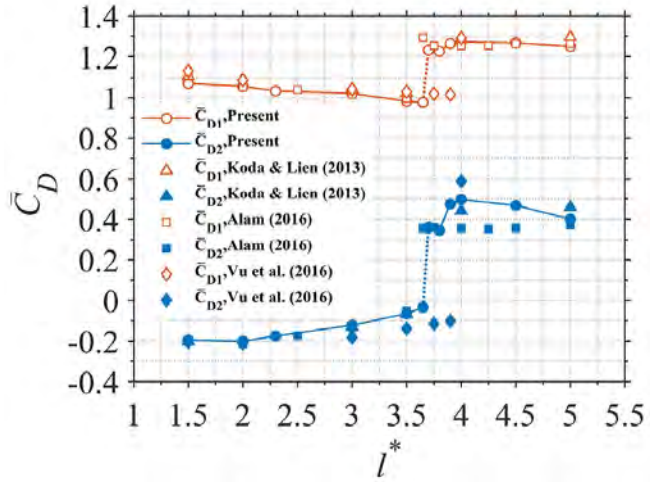

(a)

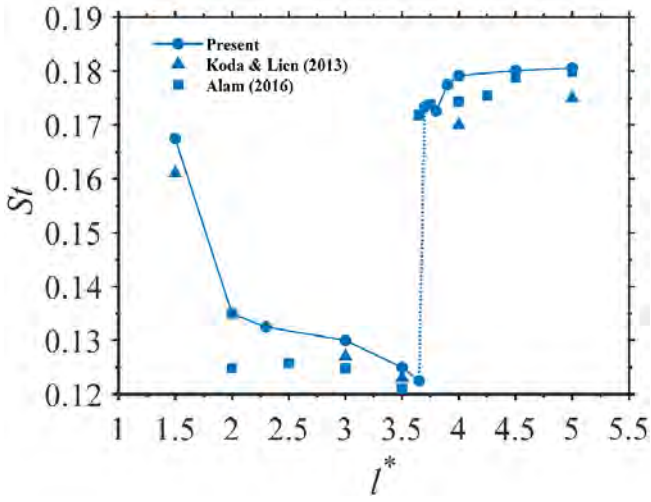

(b)

3 Validation

The procedure employed here is similar to that used in Shan and Sun (2021), where the correctness of the code and the accuracy of the numerical method have been verified effectively. For the integrity of the structure of the article, Figure 3 depicts the dependence of both the time-averaged drag coefficient (averaged over 800 non-dimensional time units when the flow is fully developed) and the Strouhal number of the two cylinders on l^* at Re = 200, and the results from the literature are included for comparison. Due to the 'lock-in' effect (Xu and Zhou, 2004; Zhou et al., 2019), the St values of the two cylinders are the same. Figure 4(a) shows that the calculated results are in good agreement with the results obtained by Koda and Lien (2013) and Alam (2016). In particular, the time-averaged drag coefficient of the upstream cylinder ($\bar{C}_{D1}$) is basically the same, whereas the time-averaged drag coefficient of the downstream cylinder ($\bar{C}_{D2}$) shows a small deviation after the drag inversion. Similarly, some deviations can be observed in Figure 4(b), but the variation trend is basically consistent with that in the literature.

Figure 5 Identification of the flow transition, (a) lift coefficient of the downstream cylinder (b) corresponding frequency spectrum (see online version for colours)

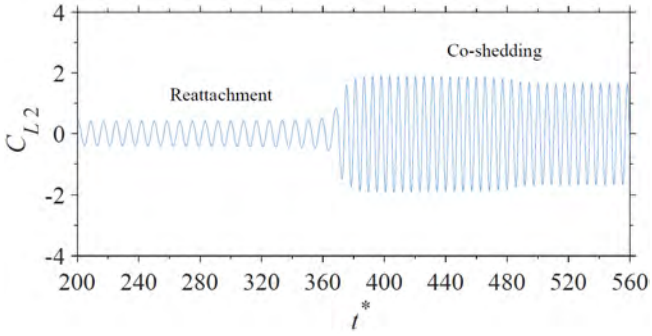

(a)

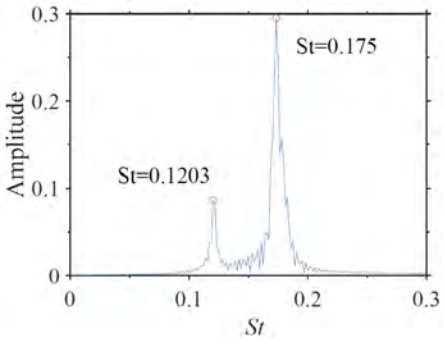

(b)

4 Results and discussion

4.1 Description of the two flow regimes

By tracking the lift signal on the downstream cylinder, a gradual transition of the two flow patterns can be seen for

Re = 200 and l^* = 3.7, as shown in Figure 5(a). Figure 5(b) shows the corresponding spectrum analysis results and uses the Strouhal number to describe the frequency changes. Two frequency components can be detected: St = 0.1203 corresponds to the reattachment regime, and St = 0.175 corresponds to the co-shedding regime. This result is similar to the experimental results of Elhimer et al. (2016) (0.1417 and 0.189) at Re = 1.66 × 10^5 and the same l^* at present, but the current values are slightly lower due to the difference in the Reynolds number. Figure 6 shows the instantaneous vorticity distribution of the two flow patterns at the moment of maximum lift in the flow. This figure reveals significant differences in the flow topology in both the gap and the wake under the two flow patterns, which show the typical flow characteristics of the reattachment regime and the co-shedding regime (see the Introduction). The convective gap vortex shedding from the upstream cylinder triggers the vortex shedding of the downstream cylinder, resulting in a binary wake (Zafar and Alam, 2018), as illustrated in Figure 6(b). In the case of the reattachment regime [Figure 6(a)], no vortex shedding occurs in the gap, and the disturbance to the downstream cylinder is weak, so a single wake is generated.

Figure 6 Vorticity field in a flow for two flow patterns, (a) reattachment regime (b) co-shedding regime (see online version for colours)

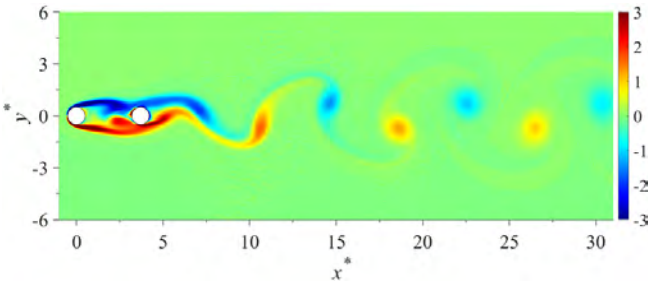

(a)

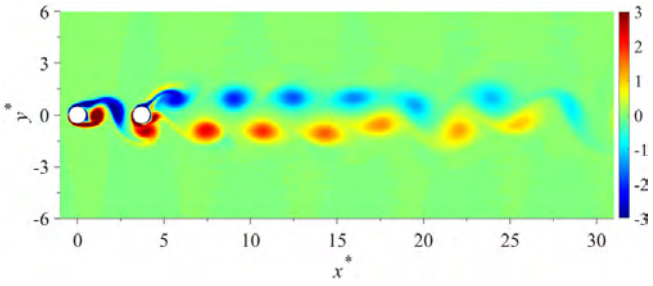

(b)

4.2 Evolution of the flow topology

4.2.1 Vorticity field

To show the transition of flow topology in the gap between the two cylinders from the reattachment flow to the co-shedding flow, we focus on the transition region where the lift coefficient changes significantly in Figure 5(a). Figure 8 shows the instantaneous vorticity distribution in the gap during the flow transition, and the corresponding snapshot of this moment is provided in Figure 7. Figure 8 demonstrates that shear layers separated from the upstream cylinder alternately reattach to the downstream cylinder surface at moment a'~c', which corresponds to the reattachment regime. Some of the reattached shear layers roll up in the gap, which leads to an increase in the strength of vorticity within the gap region. After moment f', fully developed vortex shedding is observed in the gap, which denotes the co-shedding regime. The transitional stage between these two regimes can be observed at moments d' and e'. Since the variation in the lift coefficient is quasi-sinusoidal in time, the vorticity fields corresponding to the symmetrical time points in Figure 7 can be compared with each other. Compared with moment b', the shear layer separated from the upstream cylinder at moment d' rolls up earlier but is not yet fully developed, and a small part of the shear layer convectively moves to the back of the downstream cylinder. At moment e', the rolled-up shear layer convects downstream in the gap and impinges on the windward side of the downstream cylinder. Compared with that at moments a' and c', the strength of the convective gap vortices at moment e' is greater. Therefore, the geometry of the lower rolled-up shear layer appears sharp when the vortex impinges on the downstream cylinder and embraces the front-side surface. Based on the above analysis, the transition from the reattachment flow to the co-shedding flow is characterised by a rolled-up separated shear layer gradually moving upstream in the gap from the windward side of the downstream cylinder. At the same time, the proportion of the separated shear layer participating in the rolling-up process gradually increases, and the shear layer impinges on the surface of the downstream cylinder. The shear layer is rolled up completely before reaching the downstream cylinder, leading to the full development of vortex shedding.

Figure 7 Time history of the lift coefficient on the downstream cylinder showing the moments of the snapshots (see online version for colours)

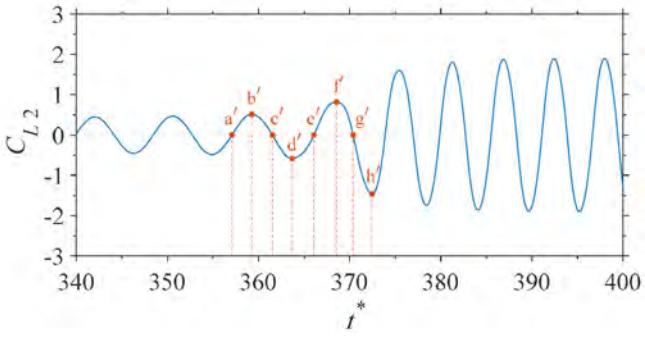

4.2.2 Flow field

Figure 9 shows the streamline distribution corresponding to each moment in Figure 7. Observing moments a'~c' in Figure 9, within the gap between the two cylinders in the reattachment regime, fluid will flow between the two quasi-static vortices and alternately flow from one side of the gap to the other. We call this kind of flow through the

gap a 'gap flow' (Shan and Sun, 2021). At the transitional stage between the two flow patterns, the most significant feature is the variation in the gap flow. As shown at moment d' in Figure 9, the gap flow becomes bidirectional at this time, i.e., the fluid first passes through the gap from the upper side to the lower side and then returns to the upper side around the quasi-static vortex near the downstream cylinder. Although there is a similar flow trend at moment b', the intensity is very weak. This 'horseshoe-shaped' gap flow alternately occurs within the gap and convects downstream, as shown in Figure 9 at moment e'. The intensity of the horseshoe-shaped gap flow is larger at moment f', and thus, the flow transitions to the co-shedding regime (see Figure 8, moment f'). With the further development of the gap flow, the flow field in the gap will eventually generate only one vortex periodically and flow downstream, as shown in Figure 9 at moments g' and h'. This analysis of the flow field shows that the evolution of the flow pattern from the reattachment flow to the co-shedding flow is characterised mainly by the variation in gap flow, i.e., the transition of the gap flow from a unidirectional flow to a horseshoe-shaped bidirectional flow.

4.2.3 Streamwise velocity

Figure 10 shows the instantaneous streamwise velocity distribution along the centreline of the two cylinders ($y^* = 0$) at the moments corresponding to the maximum (b' and f') and minimum (d' and h') lift coefficients in Figure 7. The position where the streamwise velocity changes from negative to positive is defined as the length of the recirculation bubble (Hu et al., 2019; Prsic et al., 2019; Zhang et al., 2018). As shown in Figure 10, the flow in the gap at moments b' and d' is not fully developed, which is consistent with the result in Figure 8. The size of the re-circulating bubble is approximately $L_r \approx 2$ at moment f' and shrinks at h'. This change in the streamwise velocity is consistent with the development of the gap flow in Figure 9. In addition, the recovery of the deficit flow behind the downstream cylinder increases approximately monotonically during the flow transition, while the minimum flow velocity inside the gap decreases monotonically.

4.3 Transient dynamic properties

4.3.1 Instantaneous pressure

To research the variations in the mechanical properties of the two cylinders, Figure 11 depicts the instantaneous circumferential pressure distributions corresponding to the maximum and minimum lift coefficients in Figure 7. The angle θ is measured at the nominal front stagnation point of the two cylinders, as shown in Figure 2. In Figure 11(a), there are few differences in the pressure distribution of the upstream cylinder at moments b' and d'. Figure 9 shows that this is because the gap flow has the same trend at this time and has a relatively small impact on the upstream cylinder. At moment f', since the strength of the horseshoe-shaped gap flow is larger at this time and the flow transitions to the co-shedding regime, the circumferential pressure changes remarkably. The pressure of the cylindrical surface corresponding to 69°~165° escalates, while the pressure corresponding to 165°~283° declines. With the further development of the gap flow, the upstream cylinder reaches the minimum pressure at $\theta \approx 69°$ at moment h'.

The difference in the circumferential pressure on the downstream cylinder is more obvious than that on the upstream cylinder, as shown in Figure 11(b). Moment b' corresponds to the reattachment regime, and there is a peak at $\theta \approx 49°$, which represents the reattachment point of the shear layer that has separated from the upstream cylinder (Zhou et al., 2019) and denotes the action point of the unidirectional gap flow [see Figure 9(b)]. Moment d' is in the transitional stage, at this time, the gap flow develops into a horseshoe-shaped bidirectional flow, and the peak position near $\theta \approx 308°$ represents the action point of the bidirectional gap flow. Since the bidirectional gap flow is weak at the early onset stage, the peak value is comparable to that at moment b'. At moments f' and h', the flow enters the co-shedding regime. Since the bidirectional gap flow is fully developed at this time, the peak value increases greatly near $\theta \approx 42°$ and $\theta \approx 320°$. Comparing the instantaneous curves at moments b' and f' with those at moments d' and h', respectively, shows that the peak position has a tendency to move toward the front stagnation point during the flow transition. Further examination of the instantaneous circumferential pressures of the two cylinders suggests that the transition of the flow has a considerable impact on the pressure distributions of the two cylinders, especially for the downstream cylinder. This is mainly related to the development of the gap flow.

4.3.2 Phase relationship

Figure 12 shows the time history curves of the lift coefficients of two cylinders near the transition region in the flow. For the convenience of comparison, the lift coefficient of the downstream cylinder is scaled by $\rho u_\infty^2/2$. A phase lag is evident between the fluctuating lift coefficients of the two cylinders in the reattachment regime, and the phase difference is approximately 0.25π (T/4). When the flow transitions to the co-shedding flow, the variations in the two curves are approximately in phase. This is because when the flow transitions to the co-shedding regime, the impingement of the shedding vortex from the upstream cylinder on the downstream cylinder will trigger the separation of the shear layer on the downstream cylinder and cause the lock-in effect.

4.4 Discussion

In the above analysis, we discuss the transition of the flow topology and the corresponding mechanical properties in the flow. In this section, we explore the physical mechanism leading to this flow transition.

Figure 8 Evolution of the instantaneous vorticity ($\omega_z D/u_\infty$) in the transition from reattachment flow to co-shedding flow, (a) *a′* (b) *b′* (c) *c′* (d) *d′* (e) *e′* (f) *d′* (g) *g′* (h) *h′* (see online version for colours)

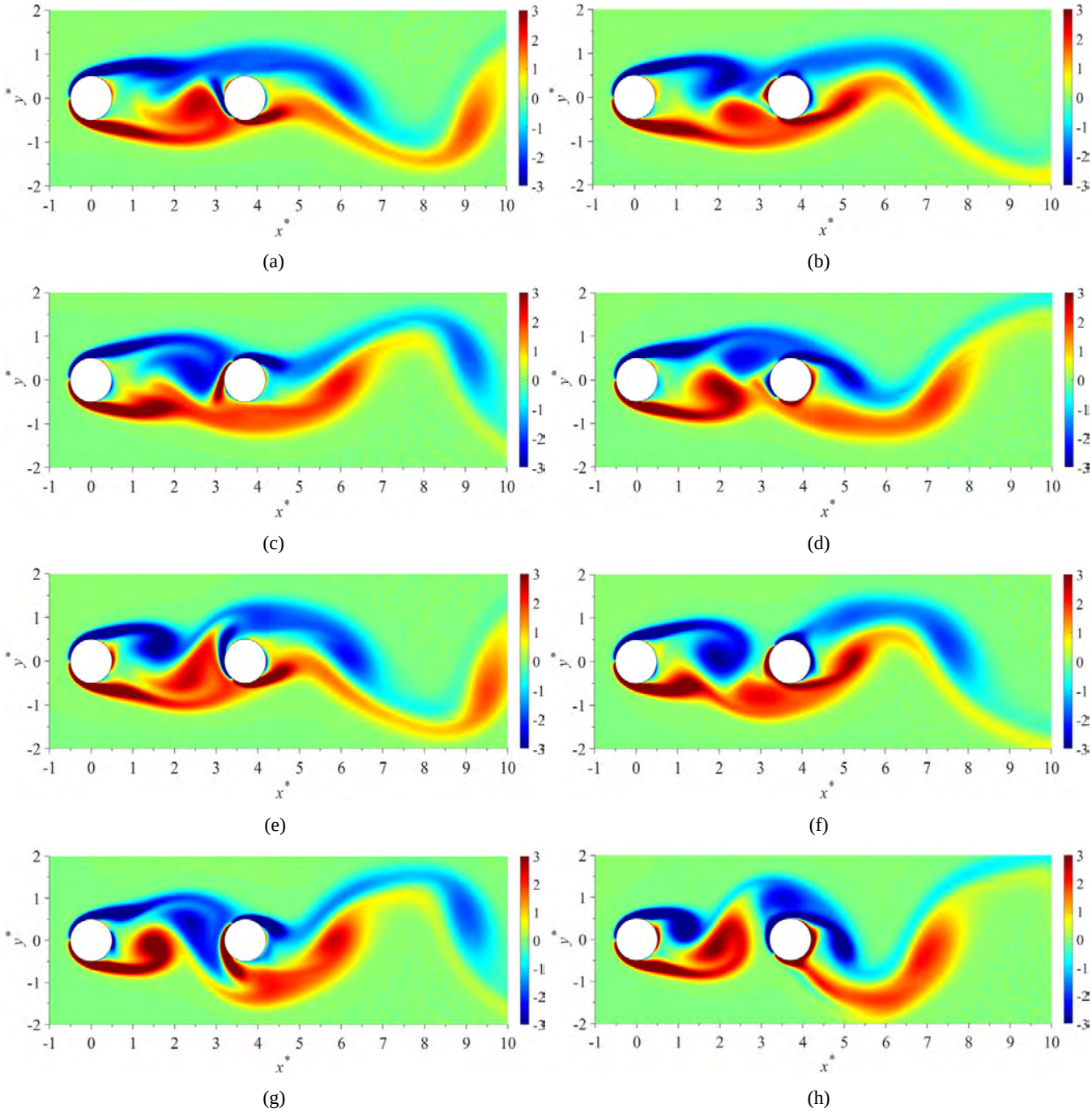

Figure 9 Evolution of the instantaneous flow field in the transition from reattachment flow to co-shedding flow, (a) *a′* (b) *b′* (c) *c′* (d) *d′* (e) *e′* (f) *d′* (g) *g′* (h) *h′* (see online version for colours)

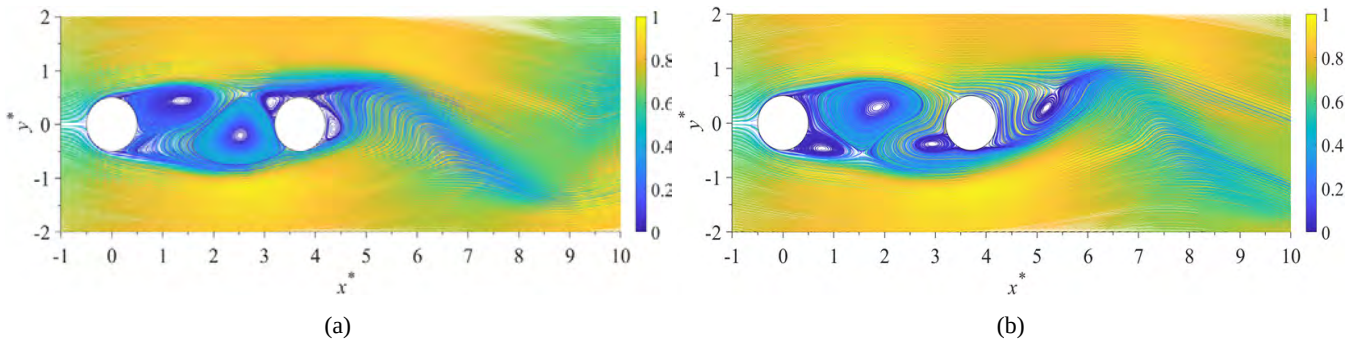

Figure 9 Evolution of the instantaneous flow field in the transition from reattachment flow to co-shedding flow, (a) *a′* (b) *b′* (c) *c′* (d) *d′* (e) *e′* (f) *d′* (g) *g′* (h) *h′* (continued) (see online version for colours)

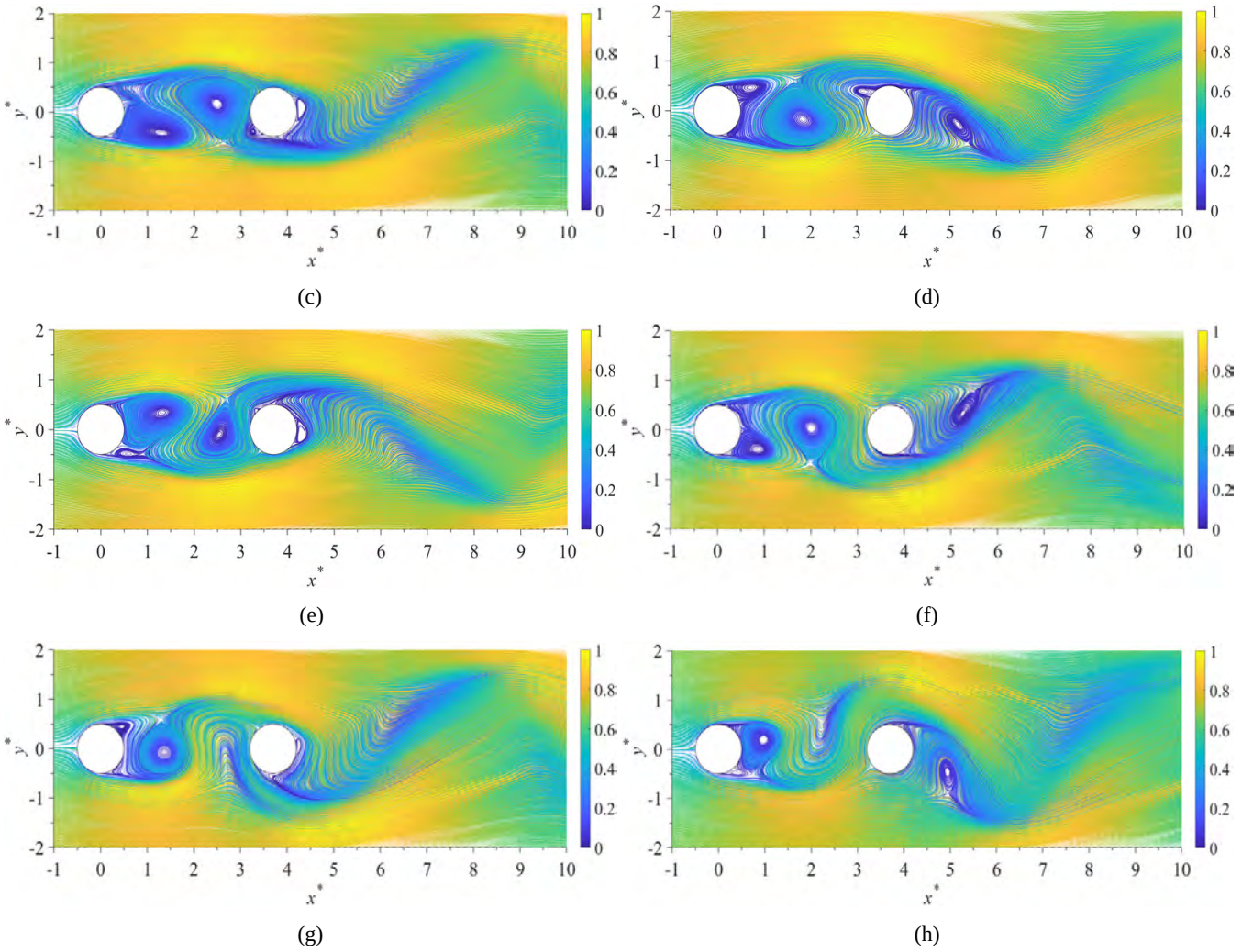

Figure 10 Instantaneous streamwise velocity along the centreline of the two cylinders (see online version for colours)

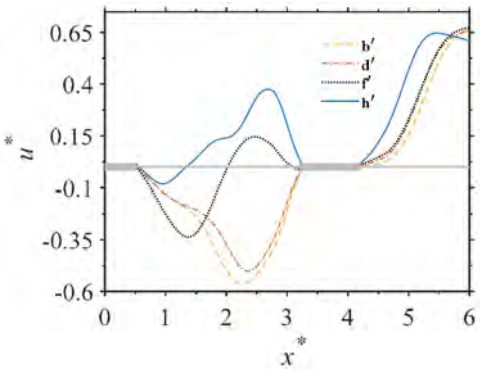

Figure 13 shows the temporal variation in the maximum lift of the downstream cylinder in the reattachment regime of the flow in comparison with that in the pure reattachment regime at $l^* = 3.65$. The figure indicates that the maximum lift in the pure reattachment regime tends to be constant after $t^* \approx 100$. However, the maximum lift in the reattachment regime at $l^* = 3.7$ increases monotonically throughout the process, although the rate of increase (slope) with time is slow after $t^* \approx 100$. This phenomenon indicates that there is a developing process for the flow transition, which occurs only when the flow develops to a certain state. This process is related to the development of the gap flow.

Due to the asymmetric separation of the shear layer from the upstream cylinder (Schewe and Jacobs, 2019), the separated shear layer, which is biased toward the centreline of the two cylinders, reattaches to the surface of the downstream cylinder due to inertia. One part is rolled up in the gap, while the remainder flows downstream. Since this asymmetric separation occurs alternately, when the separated shear layer on the other side tends toward (is biased to) the centreline, the local pressure on the same side of the gap will increase. This will induce a pressure gradient on both sides of the gap, so fluid will flow through the gap and eventually result in gap flow. With the periodic development of this process, the instability of the separated shear layer from the upstream cylinder will gradually increase at this pitch ratio. When the instability increases to a certain extent, the asymmetric flapping frequency of the separated shear layer will also increase, resulting in the

formation of a horseshoe-shaped bidirectional gap flow, under the action of which the rolling position of the separated shear layer in the gap will gradually migrate upstream from the windward side of the downstream cylinder. The shear layer rolls up completely before reaching the downstream cylinder, marking the transition to co-shedding flow.

Figure 11 Instantaneous circumferential pressure distributions of the two cylinders, (a) upstream cylinder (b) downstream cylinder (see online version for colours)

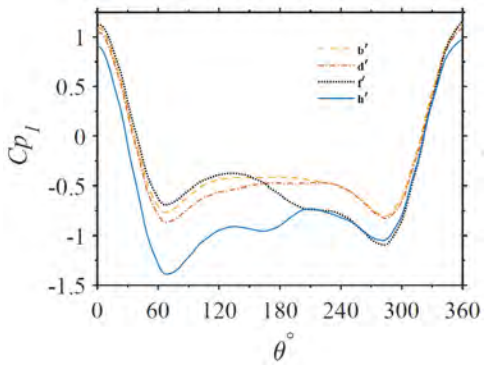

(a)

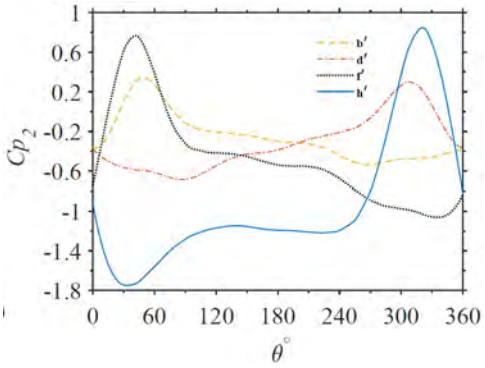

(b)

Figure 12 Phase difference between the fluctuating lift coefficients of the two cylinders (see online version for colours)

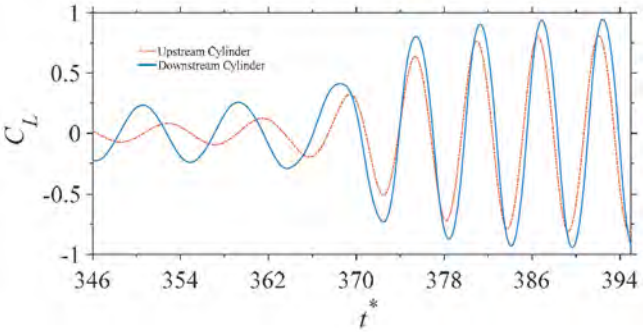

5 Conclusions

In this paper, a high-order DG method is used to study the evolution of the flow topology between two tandem cylinders from the reattachment flow to the co-shedding flow at Re = 200 and l^* = 3.7. The transient flow characteristics of the flow are studied with regard to the flow topology and dynamic properties, and the physical mechanism responsible for this evolution is explored. This paper observes for the first time that the transition of the flow from the reattachment regime to the co-shedding regime is related to the development of gap-flow, and asymmetric flow separation of the upstream cylinder is the main reason for the formation of gap-flow. The flow topology is characterised mainly by the evolution from a unidirectional gap flow to a horseshoe-shaped bidirectional gap flow. Under the action of horseshoe-shaped gap-flow, the separated shear layer from the upstream cylinder is rolled up before reaching the downstream cylinder, resulting in changes into the co-shedding regime. The development of the gap flow will increase the local pressure on the surface of the downstream cylinder, and the action point will move toward the front stagnation point during the flow transition. In addition, the phase lag of fluctuating forces acting on the two cylinders tends to decrease during the transition, and the size of the re-circulating bubble in the gap also decreases.

Figure 13 Variation in maximum lift with time in the reattachment regime on the downstream cylinder surface (see online version for colours)

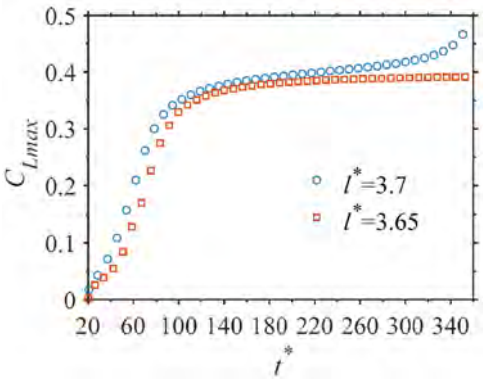

These results indicate that the DG method can be used to study the flow around two tandem cylinders with strong interference effects and can facilitate the capture of flow details due to its high numerical accuracy.

References

Alam, M.M. (2016) 'Lift forces induced by phase lag between the vortex sheddings from two tandem bluff bodies', *Journal of Fluids and Structures*, Vol. 65, pp.217–237, ISSN: 0889-9746.

Carmo, B.S., Meneghini, J.R. and Sherwin, S.J. (2010a) 'Possible states in the flow around two circular cylinders in tandem with separations in the vicinity of the drag inversion spacing', *Physics of* Fluids, Vol. 22, No. 5, pp.1–7.

Carmo, B.S., Meneghini, J.R. and Sherwin, S.J. (2010b) 'Secondary instabilities in the flow around two circular cylinders in tandem', *Journal of Fluid Mechanics*, Vol. 644, pp.395–431, ISSN: 0022-1120.

Chen, X., Li, Y.W., Drapaca, C. and Cimbala, J. (2020) 'A unified framework of continuous and discontinuous Galerkin methods for solving the incompressible Navier-Stokes equation', *Journal of Computational Physics*, Vol. 422, p.23, ISSN: 0021-9991.

Elhimer, M., Harran, G., Hoarau, Y., Cazin, S., Marchal, M. and Braza, M. (2016) 'Coherent and turbulent processes in the bistable regime around a tandem of cylinders including reattached flow dynamics by means of high-speed PIV', *Journal of Fluids and Structures*, Vol. 60, pp.62–79, ISSN: 0889-9746.

Ferrer, E. and Willden, R.H.J. (2011) 'A high order discontinuous Galerkin finite element solver for the incompressible Navier-Stokes equations', *Computers & Fluids*, Vol. 46, No. 1, pp.224–230.

Ferrero, A. and Larocca, F. (2016) 'Feedback filtering in discontinuous Galerkin methods for Euler equations', *Progress in Computational Fluid Dynamics*, Vol. 16, No. 1, pp.14–25.

Fu, G.S. and Wang, Z. (2020) 'POD-(H)DG method for incompressible flow simulations', *Journal of Scientific Computing*, Vol. 85, No. 2, p.20.

Girault, V. and Wheeler, M. F. (2008) 'Discontinuous Galerkin methods', Glowinski, R. et al (Eds.): *Computational Methods in Applied Sciences*, pp.3–26, Springer, Netherlands.

Grioni, M., Elaskar, S.A. and Mirasso, A.E. (2020) 'A numerical study of the flow interference between two circular cylinders in tandem by scale-adaptive simulation model', *Journal of Applied Fluid Mechanics*, Vol. 13, No. 1, pp.169–183.

Hesthaven, J.S. and Warburton, T. (2008) *Nodal Discontinuous Galerkin Methods: Algorithms, Analysis, and Applications*, Springer, New York.

Hu, X.F., Zhang, X.S. and You, Y.X. (2019) 'On the flow around two circular cylinders in tandem arrangement at high Reynolds numbers', *Ocean Engineering*, Vol. 189, pp.1–20, ISSN: 0029-8018.

Igarashi, T. and Suzuki, K. (1984) 'Characteristics of the flow around two circular cylinders arranged in tandem (1st report)', *Bulletin of JSME*, Vol. 24, No. 233, pp.2397–2404.

Jiang, H.Y., Cheng, L., Draper, S., An, H.W. and Tong, F.F. (2016) 'Three-dimensional direct numerical simulation of wake transitions of a circular cylinder', *Journal of Fluid Mechanics*, Vol. 801, pp.353–391, ISSN: 0022-1120.

Karniadakis, G.E., Israeli, M. and Orszag, S.A. (1991) 'High-order splitting methods for the incompressible Navier-Stokes equations', *Journal of Computational Physics*, Vol. 97, No. 2, pp.414–443.

Koda, Y. and Lien, F.S. (2013) 'Aerodynamic effects of the early three-dimensional instabilities in the flow over one and two circular cylinders in tandem predicted by the lattice Boltzmann method', *Computers & Fluids*, Vol. 74, pp.32–43, ISSN: 0045-7930.

Lin, J.C., Yang, Y. and Rockwell, D. (2002) 'Flow past two cylinders in tandem: instantaneous and averaged flow structure', *Journal of Fluids and Structures*, Vol. 16, No. 8, pp.1059–1071.

Meneghini, J.R., Saltara, F., Siqueira, C.L.R. and Ferrari, J.A. (2001) 'Numerical simulation of flow interference between two circular cylinders in tandem and side-by-side arrangements', *Journal of Fluids and Structures*, Vol. 15, No. 2, pp.327–350.

Mizushima, J. and Suehiro, N. (2005) 'Instability and transition of flow past two tandem circular cylinders', *Physics of Fluids*, Vol. 17, No. 10, pp.104–107.

Niroobakhsh, Z., Emamy, N., Mousavi, R., Kummer, F. and Oberlack, M. (2017) 'Numerical investigation of laminar vortex shedding applying a discontinuous Galerkin finite element method', *Progress in Computational Fluid Dynamics*, Vol. 17, No. 3, pp.131–140.

Prsic, M.A., Ong, M.C., Pettersen, B. and Myrhaug, D. (2019) 'Large Eddy simulations of flow around tandem circular cylinders in the vicinity of a plane wall', *Journal of Marine Science and Technology*, Vol. 24, No. 2, pp.338–358.

Riviere, B. (2008) *Discontinuous Galerkin Methods for Solving Elliptic and Parabolic Equations: Theory and Implementation*, SIAM, Philadelphia.

Schewe, G. and Jacobs, M. (2019) 'Experiments on the flow around two tandem circular cylinders from sub-up to transcritical Reynolds numbers', *Journal of Fluids and Structures*, Vol. 88, pp.148–166, ISSN: 0889-9746.

Shan, X. and Sun, F. (2021) 'Evolution of the flow structure in the gap and near wake of two tandem cylinders in the AG regime', *Fluid Dynamics*, Vol. 56, No. 3, pp.3–15.

Singha, S. and Sinhamahapatra, K.P. (2010) 'High-resolution numerical simulation of low reynolds number incompressible flow about two cylinders in tandem', *Journal of Fluids Engineering Transactions of the ASME*, Vol. 132, No. 1, pp.1–10.

Wang, R., Zhu, H.B., Bao, Y., Zhou, D., Ping, H., Han, Z.L. and Xu, H. (2019) 'Modification of three-dimensional instability in the planar shear flow around two circular cylinders in tandem', *Physics of Fluids*, Vol. 31, No. 10, pp.1–16.

Xu, G. and Zhou, Y. (2004) 'Strouhal numbers in the wake of two inline cylinders', *Experiments in Fluids*, Vol. 37, No. 2, pp.248–256.

Yang, W.C. and Stremler, M.A. (2019) 'Critical spacing of stationary tandem circular cylinders at Re approximate to 100', *Journal of Fluids and Structures*, Vol. 89, pp.49–60, ISSN: 0889-9746.

Zafar, F. and Alam, M.M. (2018) 'A low Reynolds number flow and heat transfer topology of a cylinder in a wake', *Physics of Fluids*, Vol. 30, No. 8, pp.1–18.

Zdravkovich, M.M. (1985) 'Flow induced oscillations of two interfering circular cylinders', *Journal of Sound and Vibration*, Vol. 101, No. 4, pp.511–521.

Zdravkovich, M.M. (1987) 'The effects of interference between circular cylinders in cross flow', *Journal of Fluids and Structures*, Vol. 1, No. 2, pp.239–261.

Zdravkovich, M.M. and Pridden, D.L. (1977) 'Interference between two circular cylinders; series of unexpected discontinuities', *Journal of Wind Engineering and Industrial Aerodynamics*, Vol. 2, No. 3, pp.255–270.

Zhang, F., Cheng, J. and Liu, T.G. (2020) 'A reconstructed discontinuous Galerkin method for incompressible flows on arbitrary grids', *Journal of Computational Physics*, Vol. 418, pp.1–22, ISSN: 0021-9991.

Zhang, F., Liu, T.G. and Liu, M.B. (2021) 'A third-order weighted variational reconstructed discontinuous Galerkin method for solving incompressible flows', *Applied Mathematical Modelling*, Vol. 91, pp.1037–1060, ISSN: 0307-904X.

Zhang, W., Dou, H.S., Zhu, Z.C. and Li, Y. (2018) 'Unsteady characteristics of low-Re flow past two tandem cylinders', *Theoretical and Computational Fluid Dynamics*, Vol. 32, No. 4, pp.475–493.

Zhou, Q., Alam, M.M., Cao, S.Y., Liao, H.L. and Li, M.S. (2019) 'Numerical study of wake and aerodynamic forces on two tandem circular cylinders at Re = 1000', *Physics of Fluids*, Vol. 31, No. 4, pp.1–16.

Zhou, Y. and Alam, M.M. (2016) 'Wake of two interacting circular cylinders: a review', *International Journal of Heat and Fluid Flow*, Vol. 62, pp.510–537, ISSN: 0142-727X.